

Microstructural influences on strengthening in a naturally aged and overaged Al–Cu–Li–Mg based alloy

Henry Ovri^{a,*}, Eric A. Jägle^b, Andreas Stark^c, Erica T. Lilleodden^a

^a Helmholtz Zentrum Geesthacht, Institute of Materials Research, Materials Mechanics, 21502 Geesthacht, Germany

^b Max-Planck-Institut für Eisenforschung GmbH, Department of Microstructure Physics and Alloy Design, 40237 Düsseldorf, Germany

^c Helmholtz Zentrum Geesthacht, Institute of Materials Research, Materials Physics, 21502 Geesthacht, Germany

ARTICLE INFO

Article history:

Received 19 January 2015

Received in revised form

5 March 2015

Accepted 15 April 2015

Available online 23 April 2015

Keywords:

TEM

APT

Al–Li–Cu alloys

Precipitates

Strengthening mechanisms

ABSTRACT

A combination of transmission electron microscopy, atom probe tomography and high-energy X-ray diffraction was employed to investigate the influence of local microstructural changes on strengthening in a commercial Al–Cu–Li–Mg based alloy, AA2198, in the stretched and naturally aged, and overaged states. Strengthening in the stretched and naturally aged temper was shown to be governed by a combination of Cu–Cu clusters, δ'/β' phase and solution strengthening. This is in contrast to another report which suggests that strength in this temper is only due to Cu-rich clusters [B. Decreus, et al., *Acta Mater.*, 61 (2013) 2207]. On the other hand, although large volume fractions of equilibrium phases such as T_B , and θ were present in the overaged temper, its strengthening was largely governed by order hardening, which is the strengthening mechanism associated with the δ'/β' phase. The δ'/β' phase remained in the matrix even after extensive overaging.

© 2015 Elsevier B.V. All rights reserved.

1. Introduction

Al–Cu–Li–Mg based alloys of the latest generation exhibit an excellent combination of low density, high elastic modulus and high specific strength, which makes them candidate structural materials for next generation aerospace applications [1–4]. The attractive properties of these alloys are associated with the addition of Li which not only results in significant weight reduction but also enables the formation of several strengthening precipitates including δ' (Al_3Li), δ ($AlLi$), T_1 (Al_2CuLi), T_2 (Al_5CuLi_3) and T_B (Al_7Cu_4Li). Other precipitates that have been reported in these alloys include GP zones, θ' (Al_2Cu), θ (Al_2Cu), Ω (Al_2Cu), S' (Al_2CuMg), and β' (Al_3Zr) [3–8]. The concentration and thermomechanical treatment given to a particular alloy dictates which of these precipitates forms in the alloy and ultimately determines its properties.

Recent studies of Al–Cu–Li–Mg-based alloy systems have focussed on AA2198 [9–12] which has shown an outstanding combination of static strength and damage tolerance along with good weldability and is therefore envisaged as a replacement for the AA2024/AA7475 alloys presently used in fuselage skin applications in commercial aircrafts [13,14]. Although the peak aged (PA) temper of this alloy is of application interest, detailed investigation of the structure–property relationships of other temper states is required since it provides the basis

for understanding the influence of process-induced microstructural changes on the post-processing properties of the alloy. For instance, it was shown that the T_1 precipitate, which is the main strengthening phase in the PA temper [1,12], dissolves, while T_B phase precipitates within the grain interior and in grain boundaries during friction stir welding of peak aged AA2198 [15]. The T_B phase is an equilibrium phase that occurs only in the overaged temper of Al–Li based alloy systems [8]. It was also shown elsewhere [16] that Portevin–Le Chatelier (PLC) type plastic instability, a phenomenon associated with strain localisation and reduction in ductility [17], occurs in the overaged (OA) temper of this alloy. This phenomenon refers to continuous yielding that occurs during plastic deformation, i.e. prior to necking and it manifests macroscopically as serrations (stress drops) in the plastic region of stress–strain curves. This is in addition to the significant reduction in strength that accompanies overaging. Similarly, it was recently concluded that the stretched and naturally aged (NA) temper of AA2198 must be strengthened by Cu-rich clusters, since no precipitates were observed in selected area diffraction (SAD) or dark field (DF) transmission electron microscope (TEM) micrographs [1]. It is not clear from these studies if these clusters are associated with Mg or Li. Cu–Mg co-clusters form easily during room temperature ageing of a number of Al–Cu–Mg–(Li) alloy systems and are known to confer significant strengthening [18,19]. 1st nearest neighbour distribution (1NN) analysis of atom probe tomography (APT) data of this temper state revealed only a slight deviation from the random distribution of Cu in the matrix [20]. Whether such minor deviations can sufficiently

* Corresponding author. Tel.: +49 4152 872607; fax: +49 4152 872625.

E-mail address: henry.ovri@hzg.de (H. Ovri).

account for the remarkably high strength observed in this temper is an open question.

In this paper, we present a detailed study of the microstructure–property relationship of an AA2198 alloy in the stretched and naturally aged (NA) and overaged (OA) states where the T_1 phase is absent. A systematic approach involving TEM methods, high-energy X-ray diffraction (HEXRD) and APT was adopted.

2. Materials and methods

The nominal composition of the AA2198 alloy used in the present study is given in Table 1. The alloy was received in the T351 state, that is, it had been solution treated, water quenched, stretched to a strain of 2% and naturally aged for several months. The as-received temper is hereafter referred to as NA. An artificial aging protocol aimed at achieving the overaged state (OA) within a reasonable ageing time was established on the basis of the time–temperature–precipitation diagrams proposed by Chen and Bhat [21] for a similar alloy, AA2195. The protocol comprised aging at 370 °C for 10 h.

The mechanical response of the investigated tempers was determined from tensile tests conducted at a strain rate of 5×10^{-5} /s in a Zwick universal testing station equipped with a non-contact extensometer. Dog-bone shaped samples with gauge length of 11 mm and thickness of 0.6 mm, produced by wire-cut electro-discharge machining, were used in the tensile tests.

Microstructural characterisation was conducted in large part through TEM analysis using a Philips CM200 TEM and a JEOL 3010 microscope operated at 200 kV and 300 kV, respectively. A set of the TEM samples used in the analysis was prepared by electropolishing in a twin-jet device with a solution of 67% methanol and 33% nitric acid at a temperature of -20 °C and current of 12 V, while another set was produced by focused ion beam (FIB) milling in a Nova 200 Nanolab dual-beam scanning electron microscope (SEM) from FEI, Co. The thickness of the FIB-milled lamellae was measured in the SEM prior to examination in the TEM and used as the basis for determining the average volume fraction of the δ'/β' phase. The reported volume fraction of the δ'/β' phase is the average estimated from three different micrographs, while its precipitate size is the average of over 180 precipitates imaged in a series of micrographs.

Complementary microstructural characterisation using high-energy x-ray diffraction (HEXRD) was carried out at the HZG beamline HEMS at the Deutsches Elektronen-Synchrotron (DESY) in Hamburg, Germany [22]. Samples with height of 4 mm were measured in transmission using a beam cross section of $1 \text{ mm} \times 1 \text{ mm}$. The samples were penetrated with high-energy X-rays with a photon energy of 100 keV, which corresponds to a wavelength, λ , of 0.124 Å. The resulting Debye–Scherrer diffraction rings were recorded on a 2-dimensional Perkin Elmer XRD 1622 detector with an exposure time of 0.1 s. In order to reduce background noise, 40 images were summed up for each sample, such that even weak peaks from phases with minor phase fractions were made visible. Conventional diffraction patterns were generated from the rings by azimuthal integration of the rings. Qualitative phase analysis was

achieved by means of simulated diffraction patterns. The lattice parameter of the aluminium phase was determined by the Gaussian fitting method.

Quantitative elemental analysis of the matrix phase and clustering therein was carried out with a LEAP 3000X HR, local electrode atom probe operating in laser mode. The specimen temperature was set to 60 K, the laser pulse energy was 0.6 nJ, the laser pulse repetition rate varied between 100 and 250 kHz, and the target evaporation rate was set to 1% [23]. The specimens were produced by a standard lift-out procedure [24] in the Nova 200 Nanolab dual beam SEM mentioned above. The final annular milling was carried out at an accelerating voltage of 5 kV and a beam current of 70 pA. Nevertheless, some Ga contamination was detected in the APT datasets, but the corresponding peaks in the mass spectrum were ignored in the concentration and cluster analysis. There were also unusually intense peaks corresponding to AlH^+ and AlH_2^+ in the mass spectrum. This impedes the correct determination of the Si concentration, because both AlH^+ and $^{28}\text{Si}^+$, and AlH_2^+ and $^{29}\text{Si}^+$ have mass-to-charge ratios of 28 and 29, respectively. In this study, the peak at 28 Da was assigned to Si while that at 29 Da was assigned to AlH_2 . 3D reconstruction was performed in the software IVAS (version 3.6.8) by Cameca using the initial tip apex radii and shank angles as determined by SEM before the experiments. Cluster analysis was performed in the software 3Depict (version 0.0.17) using the core-link algorithm. The cluster analysis parameters were determined according to the heuristic method used by Marceau [25].

3. Results

3.1. Tensile test

Fig. 1 shows the true stress, σ_t , vs. true strain, ϵ_t , response of each temper. The NA temper exhibited remarkably high yield strength, 310 MPa, about a factor of three higher than in the OA temper. PLC type – plastic instability was also observed in the OA temper. A portion of the σ_t vs. ϵ_t curve of the OA temper is magnified in the inset in Fig. 1 to more clearly reveal the stress drops associated with the plastic instability. It is noteworthy that the NA temper sustained a higher plastic strain than the OA temper even though its yield strength is about a factor of 3 higher than the latter. This observation underscores the detrimental effect of plastic instability on ductility. A plot of the work hardening rate ($d\sigma_t/d\epsilon_t$) as a function of true strain is also superimposed on Fig. 1. The very early stage of plastic deformation in the OA tempers showed significantly higher work hardening rate in comparison to the NA temper. The high work hardening rate of the OA temper however decreased rapidly, after

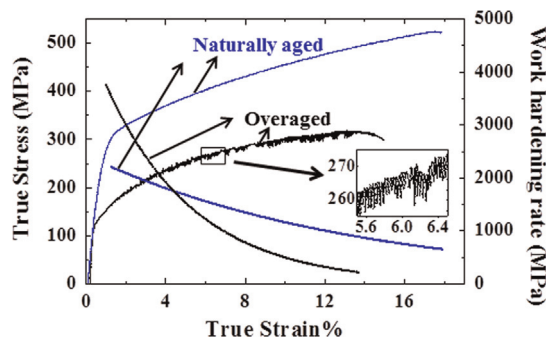


Fig. 1. (a) True stress–true strain response of AA2198 in the naturally aged (NA), in blue, and overaged (OA), in black, temper states. Plastic instabilities are observed in the overaged temper. (b) Work hardening rates ($d\sigma_t/d\epsilon_t$) of each temper plotted as a function of true plastic strain. (For interpretation of the references to colour in this figure legend, the reader is referred to the web version of this article.)

Table 1

Overall matrix concentration of the naturally aged (NA) and overaged (OA) tempers as measured from APT experiments. The concentration range given by the manufacturer (nominal) is also included in the table.

Element at%	Li	Cu	Mg	Ag	Zr	Si
Nominal	3.11–4.27	1.23–1.48	0.29–0.80	0.03–0.12	0.01–0.05	0.08
NA	3.24	1.10	0.26	0.15	–	0.28
OA	3.14	0.40	0.26	0.04	–	0.18

only about 2% plastic strain, to values lower than those obtained in the other tempers. This kind of response, namely the exceptionally high initial work hardening rate at the onset of plasticity followed quickly by a significant decrease, is typical of alloys containing a dispersion of incoherent, non-shearable second phase precipitates and is attributed to the back-stress exerted by the Orowan loops formed around the precipitates on subsequent mobile dislocations [26]. This mechanism is known to breakdown after about 2% plastic strain as a result of the plastic relaxation in the interface between the matrix and the precipitates. It is reported that geometrically necessary dislocations which are stored to accommodate the strain gradient between the deforming matrix and the non-deforming particle, drive the plastic relaxation [26]. On the other hand, the initial work hardening rates such as those found in the NA temper, have been attributed to increased strength of the dislocation junctions owing to high solute contents [10].

3.2. TEM analysis

A bright field (BF) and dark field (DF) image of the NA temper is shown in Fig. 2(a) and (b), respectively. The DF image was made from a superlattice spot characteristic of δ'/β' phase in an orientation slightly tilted away from a $\langle 100 \rangle_{Al}$ zone axis selected area diffraction (SAD) pattern. The average radius and volume fraction of the δ'/β' phase in this temper are 10 ± 5 nm and $0.004 \pm 6 \times 10^{-4}$ respectively. In contrast to this observation, Decreus [1] did not observe any precipitate in the stretched and naturally aged temper of the AA2198 alloy they investigated. In the present work, precipitates were also observed in some of the grain boundaries of the NA temper. These are likely equilibrium precipitates or disperoids that were undissolved

during the solution treatment. The absence of reflections arising from such precipitates however suggests that their volume fraction is very low. A two-beam dark field image showing the typical dislocation structure found in the NA temper is shown in Fig. 2(c). The dislocations are typically wavy, unevenly arranged, tangled and appear pinned by precipitates at several points along their line length. No evidence of dislocation pairs could be found.

In the case of the OA temper, the key microstructural features observed within the grain interior can be seen in the BF image shown in Fig. 2(d). A large spherical precipitate with radius in excess of 200 nm identified as the T_2 phase is highlighted in the micrograph. SAD patterns taken only from this precipitate (not shown) revealed the icosahedral symmetry that is associated with the T_2 phase. However, the T_2 phase was mostly found along the grain boundaries. Large T_B precipitates were also observed within the grain interior and along the grain boundaries. Faint superlattice reflections indicative of the presence of the δ'/β' phase are still evident in the $\langle 112 \rangle_{Al}$ zone axis SAD pattern inset in Fig. 2(e). Reflections associated with the T_B phase can also be seen in the SAD pattern. A DF image made from one of the superlattice spots is shown in Fig. 2(f). The average radius and average volume fraction of the δ'/β' precipitates in this phase are 11 ± 6 nm and 0.006 ± 0.002 , respectively; these values are only slightly higher than those found in the NA temper. The absence of streaks and reflections associated with the T_1 , θ' and Ω phases in the $\langle 112 \rangle_{Al}$ SAD pattern inset in Fig. 2(e) indicates that these phases, which are likely to have formed during the early stages of aging at 370 °C have dissolved, facilitating the precipitation of more equilibrium phases such as T_B phase. Time–Temperature–Transformation (TTT) diagrams proposed for a similar alloy AA2195 [21] strongly suggest that the T_1 and θ' phases

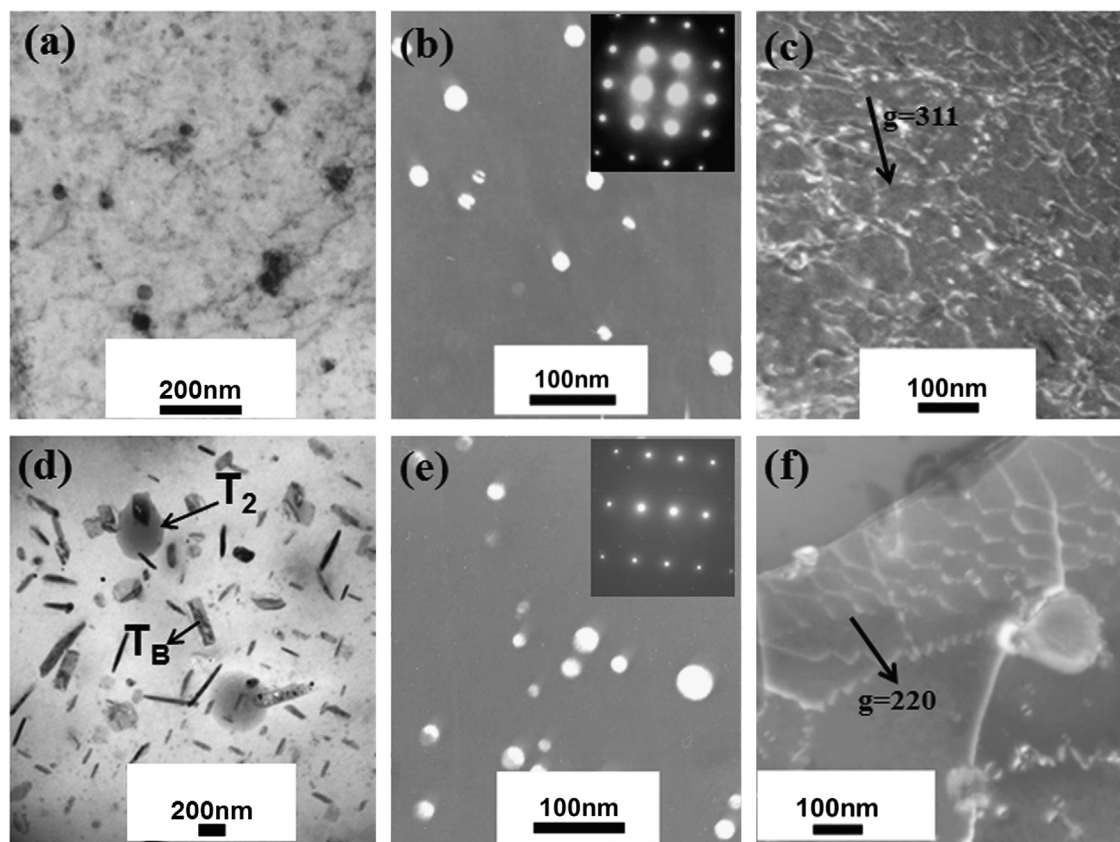


Fig. 2. : (a) Bright field and (b) dark field images of the naturally aged (NA) temper. The latter was made from a superlattice spot near the $\langle 100 \rangle_{Al}$ zone axis SAD pattern shown in the inset. δ'/β' is the only matrix precipitate present in this temper. (c) A dark field image showing the typical dislocation structure in this temper. The dislocations in this temper are wavy and homogenously distributed. (d) Bright field and (e) dark field images, showing the precipitates in the overaged (OA) temper. Several precipitates including T_2 , T_B and δ'/β' are present in the matrix of this temper (f) Typical dislocation structure found in the OA temper. The dislocations are mostly planar and only present in specific planes.

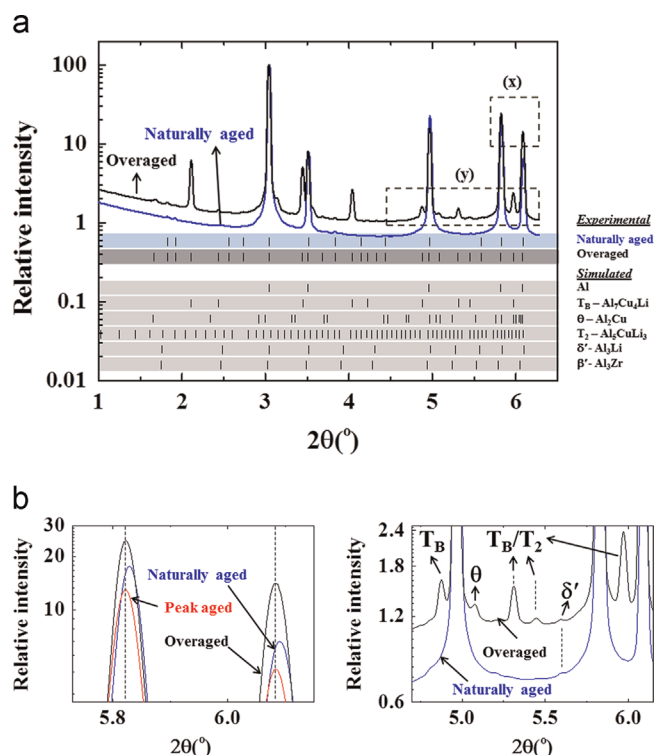


Fig. 3. (a) The full experimental HEXRD spectra of the naturally aged (NA) temper in blue and overaged (OA) in temper in black, including the 2θ positions of the experimental and simulated phases. (b) A magnified plot of the area marked *x* in (a). Two prominent experimental Al peaks showing the shift of the Al peak associated with the naturally aged in comparison with OA, peak aged (in red) and the simulated Al phase (broken line). (c) A magnified plot of the section marked *y* in (a). Peaks associated with the T_B , T_2 , θ and δ' phases can be easily identified in the plot. (For interpretation of the references to colour in this figure legend, the reader is referred to the web version of this article.)

precipitate in less than 60 s at temperatures around 204 °C and 370 °C, respectively. Fig. 2(f) shows the typical dislocation configuration found in the OA temper. The dislocations are mostly arranged in planar arrays and are uniformly distributed on individual planes. This is an indication that slip is mostly planar in this temper. It is also evident from the micrograph that the dislocations are pinned at several points around their line lengths by the δ'/β' precipitates as well as by the large precipitates. Coherent δ'/β' precipitates, as indicated by lines of no contrast perpendicular to the *g*-vector, are also observed in Fig. 2(f).

3.3. HEXRD

The full ranges of the recorded HEXRD spectra for the two tempers of interest, NA and OA, are shown in Fig. 3(a). Simulated 2θ positions of the different phases present in these tempers are included in the figure. The prominent peaks at $2\theta \approx 3.04^\circ$, 3.51° , 4.96° , 5.82° , and 6.08° for the two tempers were indexed as the Al phase. All the 2θ positions of the Al phase in the NA temper are however shifted to slightly larger 2θ values in comparison to those in the OA and simulated Al pattern. Enlarged portions of two of the Al peak positions for the NA and OA tempers are shown in Fig. 3(b) to more clearly highlight the observed shift. The corresponding peak positions for the peak aged (PA) temper and that of the simulated Al phase are also included in the plot in order to establish a reference position.

The Al phase of the simulated diffraction pattern and that of the OA and PA tempers all have a lattice parameter of 4.05 Å, while that of the NA is 4.04 Å. The uniform shifts in 2θ peak positions of

the NA temper, and the corresponding decrease in lattice parameter, relative to those of the OA and PA, are likely associated with the higher Li and Cu solute content in the NA temper. The APT analysis (see Section 3.3) shows that the matrix solute content of Li and Cu is higher in the NA temper, while the Mg content is the same in both NA and OA tempers. It has been shown that the lattice parameter of Al decreases with increasing Li, Cu, Si and Zn content, while it increases with increasing Mg content [27]. Macroscopic residual stresses arising from the 2% pre-stretch given to the NA temper prior to aging may additionally contribute to the observed decrease in lattice parameter [28]. The decrease in matrix solute concentration due to precipitation of new phases in addition to the relief of residual stresses during aging at high temperature will lead to an increase in the lattice parameter of the artificially aged tempers, i.e. the OA and PA.

An enlarged region of the HEXRD spectra showing the main phases present in the NA and OA tempers is shown in Fig. 3(c). Although five of the peaks associated with δ' coincide with the Al peak positions, it can be argued that the δ' precipitate is present in both tempers since there is a peak at $2\theta \approx 5.58$, albeit weak, that coincides with one of the simulated δ' peaks. In contrast, only two of the peaks in the experimental spectra coincide with the simulated β' peaks. However, it is not clear if β' is present in these tempers since these two peaks also coincide with the Al peak positions. Experimentally observed peaks associated with T_B , T_2 and θ phases are also highlighted in Fig. 3(c). The peaks at $2\theta \approx 5.31$ and 5.45 can be assigned to both T_B and T_2 precipitates. Close examination of the complete HEXRD spectra in Fig. 3 (a) however shows that while T_2 is present in both tempers, T_B is present only in the OA temper. Since the relative intensities of all peaks that are exclusive to the T_2 phase are similar in both tempers, it can be argued that its volume fraction is relatively constant; the T_2 phase must have thus existed prior to aging. Two such peaks can be found at $2\theta \approx 1.83$ and 1.93 . This also implies that there was negligible dissolution or formation of the T_2 phase during the heat treatment protocol employed in this investigation. On the other hand, the high intensities of the peaks associated with the T_B precipitate at $2\theta \approx 2.11$, 3.44 and 4.04 corroborate the earlier proposition that the T_B phase is the main phase that formed in the OA temper. The weak peaks at $2\theta = 2.56$ and 2.73 in both tempers could not be indexed with the simulated patterns of the known phases used in this study.

3.4. Atom probe tomography (APT)

Fig. 4 shows 10 nm thick slices through reconstructed APT dataset measured from the NA and OA tempers. Data obtained for the main solute elements, Li, Cu and Mg are shown separately. Except for a Cu-rich precipitate at the very top of the NA specimen, no other precipitates were captured in the examined tips. The inability to capture the main precipitate phase, i.e. δ'/β' phase, which was observed in both the TEM and HEXRD investigation can be attributed to the relatively low volume fraction and the large inter-particle spacing (≈ 78 nm) of this phase in the investigated tempers, relative to the typical size of an APT dataset. A proxigram created using the interface of the Cu-rich phase (not shown) at the top of the NA specimen indicates that it is most likely an equilibrium θ precipitate. This precipitate, like the T_2 , must have been undissolved in the solution treating step. The elemental distribution of atoms in both tempers seems to be homogenous and there is no visible evidence of clustering of any of the elements. A good indication of solute clustering is nevertheless obtained by the use of cluster identification algorithms [29]. In preparation for cluster analysis, regions not belonging to the matrix phase were removed from the datasets. This included the Cu-rich precipitate from the NA temper sample and a crystallographic pole (an APT measurement artefact) to

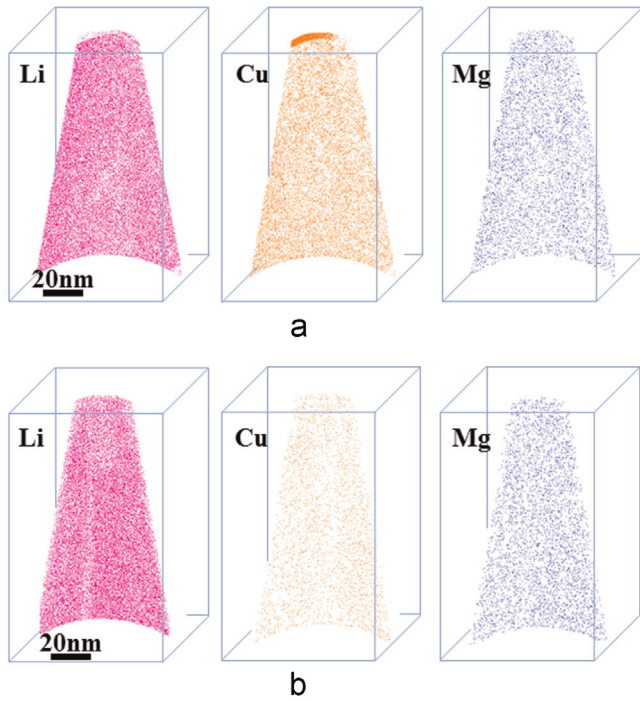


Fig. 4. 3D APT maps of Li (pink), Cu (orange), and Mg (blue) atoms in (a) the naturally aged (NA) temper and (b) the overaged (OA) temper. With the exception of a Cu-rich phase at the tip of the NA temper, no precipitate was visible in all the measurements. More so, all the atoms are seemingly homogeneously distributed. (For interpretation of the references to colour in this figure legend, the reader is referred to the web version of this article.)

which Cu atoms segregated slightly from the OA temper sample. In this work, the core-linkage (CL) algorithm technique was employed. The CL technique is a variation of the Density Based Clustering technique, in which clusters are defined as areas having a density higher than the remainder of the matrix. More details about the method can be found in literature [29]. The d_{core} and d_{link} parameters which define the CL algorithm were determined using an approach recently employed by Marceau [25]. Specifically, d_{core} was set to the distance at which the difference between cumulative 5th nearest neighbour distances (5NN) and its randomized counterpart was the highest ($d_{\text{core}} = 1.58$ nm and 2.35 nm for Cu–Cu atoms in the NA and OA tempers respectively), while d_{link} was set to $\frac{1}{2} d_{\text{core}}$. Only clusters consisting of at least 3 atoms were considered. The random data was generated from the experimental data; only the chemical identities of the atoms were randomized, their spatial positions were unchanged. 5NN frequency histograms of the main alloying elements, namely, Li–Li, Cu–Cu, Mg–Mg and Cu–Mg in the NA and OA tempers and their respective randomized distributions are presented in Fig. 5. Evidence of clustering, indicated by the broadening and shifting of the distribution maxima of the experimental 5NN histogram, relative to the randomized 5NN histogram, to smaller distances [29,30], can mainly be seen between the Cu–Cu atoms in the NA and OA tempers. A slight shift of the distribution maxima can also be observed between the experimental and random 5NN histograms of the Li–Li atoms in both tempers. Further analyses with the CL technique, which is a more accurate and efficient cluster identification technique [29], however show that significant clustering, exceeding what can be found in a randomized dataset, only occurred between the Cu–Cu atoms in the NA temper. The size distribution of the Cu–Cu clusters determined by the CL technique is plotted as a function of cluster size in Fig. 6 for both the NA and the OA tempers. There is a significant difference between the Cu–Cu cluster size distributions for the experimental and the randomized datasets of the NA temper but there is practically no difference

between these distributions in the OA temper. Additionally, there is a significantly higher density of detected Cu–Cu clusters in the NA temper ($1.25 \times 10^{25} \text{ m}^{-3}$) in comparison to the OA temper ($1.69 \times 10^{24} \text{ m}^{-3}$). Together these results are a strong indication that the contribution of the clusters to strength will be much higher in the NA temper than in the OA temper. On the other hand, no difference was observed between the number of CL-detected Li–Li clusters in the experimental and in the randomized datasets in both tempers. This indicates that Li–Li clusters do not form in the NA and OA tempers of AA2198.

The overall matrix concentration of the main alloying elements of the NA and OA tempers obtained from the APT measurements is given in Table 1. Over six million atoms were captured in each test. Atoms of Zr were not detected in the measurements, probably because of its very low concentration in the alloy and because most of the Zr atoms might be located in Al_3Zr precipitates. Additionally, the location of the Zr^{2+} peaks in the “thermal tail” of the main Al^+ peak leads to a higher noise level in the mass-to-charge spectrum and hence complicates the accurate detection of the Zr atoms. Si was overestimated in both samples. The probable cause of this, the overlap between Si and AlH_n peaks, has been explained earlier. Regardless, the experimental concentrations of the main alloying elements are comparable with the nominal concentration and can therefore be taken as good indication of the global matrix concentration of this alloy after ageing. A significant decrease in the matrix Cu concentration of the OA temper relative to that of the NA temper was recorded. This large decrease, of about 64%, is associated with the formation of the high volume fraction of large equilibrium Cu-rich precipitates, such as T_B , in the overaged state. The high peak intensity of the T_B precipitate as seen in the HEXRD spectra is a clear indication that its volume fraction is high in the OA temper. The matrix Li concentration in the OA temper was only slightly less than that of the NA temper. It can be argued that although the TEM and HEXRD analyses show that the T_B phase is present in significant amounts, its presence is not expected to lead to a significant depletion of Li from the matrix considering that the percentage composition of Li in T_B is only 1.54%. The Mg concentration remained unchanged.

4. Discussion

The preceding microstructural analyses indicate that there are a number of obstacles to dislocation glide in the investigated tempers. The mechanical behaviour of each temper is nonetheless governed by the obstacle that provides the greatest resistance to dislocation glide. The obstacle governing strength in each temper, i.e. NA and OA, is now investigated by invoking known relations for estimating the theoretical strength provided by the obstacles observed in these tempers.

Major sources of strengthening in the NA temper include the δ'/β' precipitate revealed by both TEM and HEXRD, Cu–Cu solute clusters revealed by the APT measurements and matrix solute atoms. It is well established that strengthening by the δ' phase, which is a long-range ordered phase, is due to order hardening; a mechanism that leads to the creation of an antiphase boundary (APB) on the slip plane of an ordered coherent precipitate upon shearing by matrix dislocations [31,33]. The energy of the APB represents the resistance that must be overcome by the matrix dislocations for slip to occur. The theoretical critical resolved shear stress (CRSS) predicted by order hardening τ^{OH} , can be estimated from [36]

$$\tau^{OH} = \frac{\gamma_{\text{apb}} f^{\frac{1}{2}}}{2b} \left[1.731 \left(\frac{\pi \gamma_{\text{apb}} b_0}{4Gb^2} \right)^{\frac{1}{2}} - f^{\frac{1}{2}} \right], \quad (1)$$

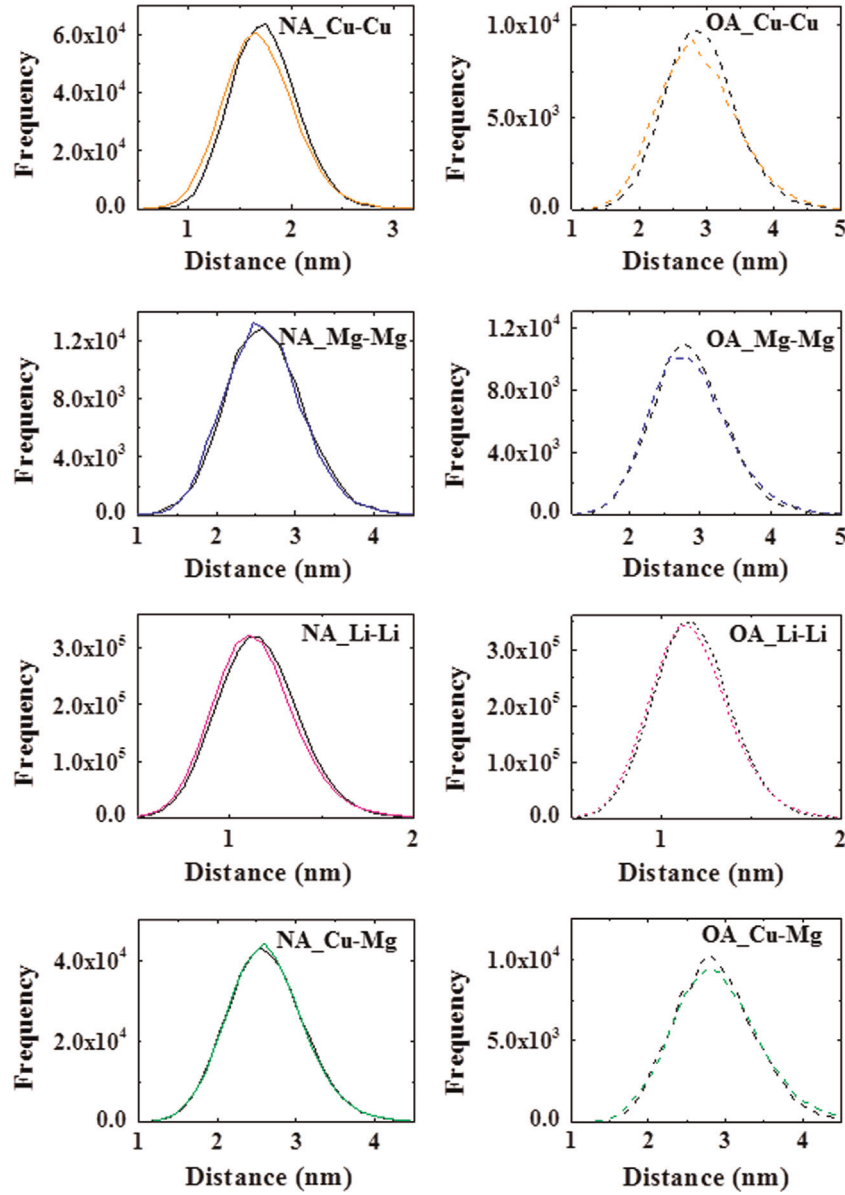


Fig. 5. Frequency histograms of 5th nearest neighbour distances (5NN) between atoms of the naturally aged (NA) temper, in straight lines and the overaged (OA) temper, in broken lines. The distribution of the main atomic species, Li–Li (pink), Cu–Cu (orange), Mg–Mg (blue), Cu–Mg (green) and their respective randomised distribution (black) are also presented. (For interpretation of the references to colour in this figure legend, the reader is referred to the web version of this article.)

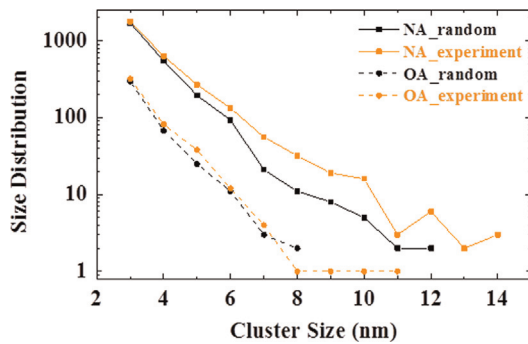


Fig. 6. The size distribution of the Cu–Cu clusters in the naturally aged, NA, (straight orange line) and overaged, OA, (broken orange line) tempers. The respective randomised distribution for the NA (straight black line) and OA (broken black line) tempers is also included in the plot. (For interpretation of the references to colour in this figure legend, the reader is referred to the web version of this article.)

where γ_{apb} is the antiphase boundary energy, G is the shear modulus, b is the Burgers vector, r_o is the average precipitate radius and f the volume fraction of the precipitates. Since it was not possible in this work to clearly distinguish between the δ'/β' precipitates, the CRSS, τ^{OH} , was estimated with the well-known order hardening parameters for δ' . This approach is considered to be reasonable even in the case of δ'/β' core-shell precipitates since the core-shell interface has been shown to be coherent, with the atomic planes bending only slightly across the interface [34]. Using the Taylor factor of 2.95 [18], $G=30 \text{ GN m}^{-2}$ [32], $b=0.2864 \text{ nm}$ [32], $\gamma_{\text{apb}}=0.15 \text{ J m}^{-2}$ [32], and the experimentally determined values of $r_o=10 \text{ nm}$ and $f=0.004$, the theoretical yield strength due to order hardening, σ_y^{OH} , is found to be 55 MPa for the NA temper. The experimentally found yield strength for this temper is 310 MPa. It follows that order hardening is not the governing strengthening mechanism in this temper.

The contribution to strength from the unclustered atoms of the main alloying elements, i.e., Li, Cu and Mg, in the matrix of the NA temper was determined from the classical relationships given in Eqs. (2) and (3) [35]. These relationships predict the contribution to solution strengthening from the size misfit interaction, τ^{EI} and the modulus misfit interaction, τ^{MI} . The CRSS due to solution strengthening, τ^{SS} , from a solute element, x , is equal the sum of Eqs. (2) and (3).

$$\tau^{\text{EI}} = 1.26G (0.1\epsilon_a)^{4/3} c_x^{2/3}, \quad (2)$$

$$\tau^{\text{MI}} = 1.26G \left[\frac{1}{32\pi^2} \epsilon_G \left(1 + \frac{\epsilon_G}{2} \right)^{-1} \right]^{4/3} c_x^{2/3}. \quad (3)$$

The term c_x in Eqs. (2) and (3) is the concentration of the solute element, while ϵ_G and ϵ_a are the size misfit and modulus misfit parameters, respectively. After Marceau [25], the total CRSS due to solution strengthening, τ^{SS} , is taken as

$$\tau^{\text{SS}} = \sqrt{\tau^{\text{SS}}\text{Li}^2 + \tau^{\text{SS}}\text{Cu}^2 + \tau^{\text{SS}}\text{Mg}^2}. \quad (4)$$

The effective matrix concentration of Cu in both NA and OA tempers decreased to 0.89 and 0.25 at%, respectively, after the Cu atoms tied up in the Cu–Cu clusters were deducted from the global matrix Cu concentrations. Mg and Li did not form any cluster or co-cluster and so their matrix concentrations are effectively equal to the values in Table 1. Literature values of ϵ_G for Li, Cu and Mg are 4, 0.48 and 0.87, respectively, while the values for ϵ_a are 10^{-2} , -0.35 and 0.37 respectively [35]. With these parameters, the contribution to the yield strength of the NA temper due to Li, Cu and Mg in solution, σ_y^{SS} , is predicted to be 63 MPa. Since this value is significantly less than the experimentally observed yield strength it can be argued that strengthening in this temper is largely governed by the Cu–Cu clusters, which have been found through APT analysis to be present in large amounts. This is consistent with the conclusions made by Decreus [1] and Deschamps [12]. Nonetheless, the contributions of the other constituent obstacles, in particular the δ'/β' precipitates which were not observed in the Decreus work [1], along with the various solute atoms present in the matrix, cannot be ignored; they may contribute up to half of the total experimentally observed yield strength.

In the case of the OA temper, both TEM and HEXRD investigations reveal that several different precipitates, including T_B , T_2 , θ and δ' , are present in the OA temper. The APT cluster analysis also indicates that a small amount of Cu–Cu clusters will be present. It can be argued that the T_B precipitate has a significantly higher volume fraction than those of the other precipitate species since its HEXRD peak intensity is significantly higher than those of the other precipitate species. Although the presence of the δ'/β' phase in this temper is somewhat surprising, its continued presence can be partly attributed to its relative stability, which is a consequence of its coherency with the matrix [6]. This is supported by the work of Lee [37], which shows that the coarsening rate of δ' in Al–Li binary alloys is significantly reduced by the addition of small amounts of Ag. Similarly, Radmilovic [38] argues that L_{12} core/shell precipitates, such as δ'/β' , exhibit extremely low coarsening rates.

The main strengthening precipitate present in the OA temper is the δ'/β' phase. The contribution to yield strength from equilibrium phase precipitates such as T_B , T_2 , and θ is known to be negligibly small [39]. According to Eqs. (1) and (4), the theoretically predicted yield strength due to order hardening, σ_y^{OH} , in the OA temper is 71 MPa, while the theoretically predicted yield strength due to solute strengthening, σ_y^{SS} , is 38 MPa. Its experimental yield strength, σ_y^{exp} , is 133 MPa. Although additional contribution to strength is expected from the Cu–Cu clusters, grain boundaries and dislocations still

present in the matrix, it can be argued that order hardening governs strength in the OA temper and not Orowan hardening as is the case for overaged tempers of most precipitation strengthened alloys. It can be further argued that the strengthening from the Cu–Cu clusters in the OA temper in comparison to the NA temper will be very small because of the significantly lower number density of clusters in the former.

Although the significant difference in yield strength between the NA and OA was expected, the difference in their post-yield behaviour, and specifically the absence of plastic instability in the NA temper and its presence in the OA temper, is remarkable. The occurrence of plastic instability in Al–Li based alloys have been largely attributed to dynamic strain aging of temporarily trapped mobile dislocations by Li atoms [40–42]. This cannot however explain the absence of plastic instability in the NA temper. The APT analysis shows that the Li content of the OA temper which exhibited plastic instability is less than that of the NA temper. The result rather indicates that occurrence of plastic instability is associated with order hardening, which is the governing strengthening mechanism in the OA temper. A detailed investigation of the underlying mechanism for plastic instability in these alloy systems is presented elsewhere [16].

5. Conclusion

The effect of microstructural changes on the strengthening mechanism associated with the δ' phase in a commercial Al–Cu–Li–Mg based alloy AA2198 was investigated using a combination of tensile test, APT, HEXRD and TEM methods. In contrast to previous reports [1,12] that no precipitate is present in stretched and naturally aged (NA) AA2198, our results show that the δ'/β' precipitate is present and remains in the matrix of the alloy even after extensive overaging. Based on quantitative analyses of the contribution of the δ'/β' precipitates and the solute atoms, it was shown that up to half of the strength in the NA temper is provided by obstacles other than solute clusters. This strongly indicates that the remarkably high strength in this temper is the result of the combination of several obstacles to dislocation glide, not just the Cu–Cu solutes. On the other hand, several precipitates including T_B , T_2 , θ and δ' phase were observed in the overaged (OA) temper. It was shown, albeit qualitatively, that the T_B phase had a significantly higher volume fraction than the other phases. Based on theoretical considerations and experimentally determined parameters, it was determined that strength in the OA temper is governed by order hardening, which is the strengthening mechanism associated with δ' precipitate.

Acknowledgement

Mr. Uwe Lorenz is grateful appreciated for technical support offered while carrying out the TEM experiments. Some of the TEM investigation was carried out at the National Centre for Electron Microscopy (NCEM) at Lawrence Berkeley Laboratory, which is supported by the U.S. Department of Energy under Contract # DE-AC02-05CH11231.

References

- [1] B. Decreus, A. Deschamps, F. De Geuser, P. Donnadiou, C. Sigli, M. Weyland., *Acta Mater.* 61 (2013) 2207–2218.
- [2] E.J. Lavernia, N.J. Grant, *J. Mater. Sci.* 22 (1987) 1521–1529.
- [3] R.J. Rioja, J. Liu, *Metall. Mater. Trans. A* 43 (2012) 3325–3337.
- [4] J.W. Martin, *Ann. Rev. Mater. Sci.* 18 (1988) 101–119.
- [5] P. Donnadiou, Y. Shao, F. De Geuser, G.A. Botton, S. Lazar, M. Cheynet, M. De Boissieu, A. Deschamps, *Acta Mater.* 59 (2011) 462–472.

- [6] S.C. Wang, M.J. Starink, *Int. Mater. Rev.* 50 (2005) 193–215.
- [7] Z. Chen, K. Zhao, L. Fan, *Mater. Sci. Eng. A* 588 (2013) 59–64.
- [8] Y.S. Lee, *J. Mater. Sci. Lett.* 17 (1998) 1161–1164.
- [9] V. Araullo-Peters, B. Gault, F. De Geuser, A. Deschamps, J. Cairney, *Acta Mater.* 66 (2014) 199–208.
- [10] T. Dorin, F. De Geuser, W. Lefebvre, C. Sigli, A. Deschamps, *Mater. Sci. Eng. A* 605 (2014) 119–126.
- [11] T. Dorin, A. Deschamps, F. De Geuser, C. Sigli, *Acta Mater.* 75 (2014) 134–146.
- [12] A. Deschamps, B. Decreus, F. De Geuser, T. Dorin, M. Weyland, *Acta Mater.* 61 (2013) 4010–4021.
- [13] M. Knüver, J. Schumacher, H. Ribes, F. Eberl, B. Bes, in: *Proceedings of the 17th AeroMat Conference & Exposition*, Seattle, Washington, May 15–18, 2006.
- [14] N.D. Alexopoulos, E. Migklis, A. Stylianios, D.P. Myriounis, *Int. J. Fatigue* 56 (2013) 95–105.
- [15] J. Rao, E.J. Payton, C. Somsen, K. Neuking, G. Eggeler, A. Kostka, J.F. Dos Santos, *Adv. Eng. Mater.* 12 (2010) 298–303.
- [16] H. Ovri, E.T. Lilleodden, *Acta Mater.* 89 (2015) 88–97.
- [17] R.C. Picu, G. Vincze, F. Ozturk, J.J. Gracio, F. Barlat, A.M. Maniatty, *Mater. Sci. Eng. A* 390 (2005) 334–343.
- [18] M.J. Starink, P. Wang, I. Sinclair, P.J. Gregson, *Acta Mater.* 47 (1999) 3855–3868.
- [19] M.J. Starink, P. Wang, *Acta Mater.* 57 (2009) 2376–2389.
- [20] W. Lefebvre, K. Hoummada, B. Decreus, F. de Geuser, in: J. Hirsch, B. Skrotzki, G. Gottstein (Eds.), *Proceedings of the 11th International Conference on Al Alloys*, vol. 1, Wiley-VCH Weinheim, Aachen, Germany, 2008, pp. 801–807.
- [21] P.S. Chen, B.N. Bhat, *NASA/TM* 211548, 2002.
- [22] N. Schell, A. King, F. Beckmann, T. Fischer, M. Müller, A. Schreyer, *Mater. Sci. Forum* 772 (2014) 57–61.
- [23] B. Gault, F. de Geuser, L. Bourgeois, B.M. Gabbie, S.P. Ringer, B.C. Muddle, *Ultramicroscopy* 111 (2011) 683–689.
- [24] M.K. Müller, K.F. Russell, G.B.G.B. Thompson, *Ultramicroscopy* 102 (2005) 287–298.
- [25] R.K.W. Marceau, A. De Vaucorbeil, G. Sha, S.P. Ringer, W.J. Poole, *Acta Mater.* 61 (2013) 7285–7303.
- [26] M.F. Ashby, *Philos. Mag.* 14 (1966) 1157–1178.
- [27] H.J. Axon, W. Hume-Rothery, *Proc. R. Soc. Lond. A* 193 (1032) (1948) 1–24.
- [28] W. Reimers, A.R. Pyzalla, A. Schreyer, H. Clemens (Eds.), *Neutrons and Synchrotron Radiation in Engineering Materials Science*, Wiley-VCH, Weinheim, 2008.
- [29] B. Gault, M.P. Moddy, J.M. Cairney, S.P. Ringer, *Atom Probe Microscopy*, Springer, New York, 2012.
- [30] R.K.W. Marceau, G. Sha, R. Ferragut, A. Dupasquier, S.P. Ringer, *Acta Mater.* 58 (2010) 4923–4939.
- [31] A.J. Ardell, *Metall. Trans. A* 16 (1985) 2131.
- [32] J.C. Huang, A.J. Ardell, *Mater. Sci. Eng. A* 104 (1988) 149–156.
- [33] C. Schlesier, E. Nembach, *Acta Metall. Mater.* 43 (1995) 3983–3990.
- [34] N. Kim, J. Howe, E. Boden, *J. Phys. Colloq.* 48 (1987), C3-457–C3-463.
- [35] P. Gomiero, Y. Brechet, F. Louchet, A. Tourabi, B. Wack, *Acta Metall. Mater.* 40 (1992) 857–861.
- [36] A.S. Argon, *Strengthening Mechanisms in Crystal Plasticity*, Oxford University Press, Oxford, 2008.
- [37] B.C. Lee, J.K. Park, *Acta Mater.* 46 (1998) 4181–4187.
- [38] V. Radmilovic, A. Tolley, E.A. Marquis, M.D. Rossell, Z. Lee, U. Dahmen, *Scr. Mater.* 58 (2008) 529–532.
- [39] H.R. Shercliff, M.F. Ashby, *Acta Metall. Mater.* 38 (1990) 1789–1802.
- [40] S. Kumar, J. Król, E. Pink, *Scr. Mater.* 35 (1996) 775–780.
- [41] P.J. Gregson, D.S. McDermid, E. Hunt, *Mater. Sci. Technol.* 4 (1988) 713–718.
- [42] M. Cieslar, P. Vostrý, I. Stulíková, *Phys. Stat. Sol.* 157 (1996) 217–227.